Available online at www.sciencedirect.com
ScienceDirect
Trans. Nonferrous Met. Soc. China 32(2022) 559−568
Transactions of Nonferrous Metals Society of China
www.tnmsc.cn

Effect of Ta addition on solidification microstructure and element segregation of IN617B nickel-base superalloy

Shuang GAO[1,2], Zhen-feng SONG[1,2], Bo HE[1, 2], Lan-zhang ZHOU[3], Jie-shan HOU[3]

1. School of Material Engineering, Shanghai University of Engineering Science, Shanghai 201620, China;
2. Research Center of High-temperature Alloy Precision Forming, Shanghai University of Engineering Science, Shanghai 201620, China;
3. Institute of Metal Research, Chinese Academy of Sciences, Shenyang 110016, China

Received 11 January 2021; accepted 9 July 2021

Abstract: IN617B nickel-base superalloy is considered as a good candidate material in 700 °C advanced ultra-supercritical coal-fired power plants. The effect of Ta addition on solidification microstructure and element segregation of IN617B alloy was investigated by OM, SEM, TEM, EDS, EPMA and thermodynamic calculation. The results showed that the solidification microstructure exhibited a dendritic segregation pattern with many primary carbides distributed in interdendritic regions, such as network M_6C, lath $M_{23}C_6$ and granular Ti(C,N). The addition of Ta promoted the precipitation of Ta-rich MC significantly inhibiting the precipitation of M_6C and $M_{23}C_6$, and reduced the segregation degree of Al, Mo and Ti alloying elements. The addition of Ta decreased the melting temperature of MC carbide, but did not impact the solidification path, that was, $L\rightarrow \gamma$ matrix → MC or Ti(C,N) → M_6C → $M_{23}C_6$, where MC and Ti(C,N) tended to form symbiotic microstructure with M_6C. This study will provide theoretical basis and data support for the alloy optimization and casting structure control of IN617B nickel-based superalloy.
Key words: IN617B nickel-base superalloy; Ta addition; solidification microstructure; element segregation; carbide

1 Introduction

In recent decades, intensive development work about a new generation of advanced ultra-supercritical coal-fired (A-USC) power plants is ongoing in many countries around the world, such as EU, USA, Japan, and China [1,2]. The technology would be operated at above 700 °C and steam pressure at 35 MPa, which will enable a reduction of CO_2 emission of around 40% and an increase of net efficiency of more than 6% compared with traditional USC power plants operating today [3]. Due to the elevated service temperature, traditional materials such as ferritic/martensitic heat-resistant steels will not satisfy the requirements of A-USC power plants. Under the service condition of A-USC, the most severely thermal-exposure components, such as furnace panels, superheater turbine rotors, casings, valves, and bolts, are expected to made by Ni-based superalloy [4−6]. For example, IN617B alloy, a solid solution strengthened Ni-based superalloy, has been selected as the prime candidate for heavy castings including shells and valves in A-USC power plants because it possesses high creep rupture strength and superior high temperature corrosion resistance [7,8]. IN617B alloy is the B-alloyed variant of IN617 alloy developed by the German national project MARCKO DE2 [3,9]. WU et al [10] found that the primary particles were Ti(C, N), γ', M_6C and $M_{23}C_6$ in long-term aging IN617B alloy. The existence of further secondary phases such μ-phase [11,12] and δ-phase [13] had

Corresponding author: Jie-shan HOU, Tel: +86-24-83971911, Fax: +86-24-83978045, E-mail: jshou@imr.ac.cn
DOI: 10.1016/S1003-6326(22)65815-1

been proved to impact the thermal stability of IN617B alloy. TYTKO et al [14] considered that the addition of B was conducive to improve the thermal stability of IN617B alloy, and they deemed that the segregation of B stabilized a network of secondary $M_{23}C_6$ precipitates near grain boundaries (GBs) and thus increased the creep rupture life of IN617B alloy. The other important reason for the degradation of mechanical properties is the gradual coarsening of γ' particles in the alloy [15]. It was explained that the mean distance between the precipitates monotonously increased when the γ' particles gradual coarsened with the thermal exposure time [16,17]. As a result, the critical resolved shear stress that dislocation movement needed to overcome decreased, leading to the reduction of the material's strength [17]. In our previous research [18], it was found that the addition of Ta was beneficial for promoting the mechanical properties of IN617B alloy by refining the γ' phase and stabilizing the secondary carbides during long-term thermal exposure.

The thermal stability of the alloy during long-term service is important for materials applied in A-USC power plants. Therefore, the impact of microstructure evolution during long-term aging on the degradation of the mechanical properties of IN617B alloy gained extensive attention in the past. However, the studies about solidification microstructure and element segregation of IN617B alloy during solidification process are quite uncommon. It is important for a cast alloy to ascertain the effect of a new alloying element addition on solidification path, element segregation and solidification temperature range [19]. For nickel-base superalloys, Ta element is a strong forming element of MC carbide [20] and γ' [21,22] which did not appear in solidification microstructure of IN617B alloy. This implies that the Ta addition will change the constitute of primary phases in solidification microstructure. Moreover, it was proved that Ta addition could change the characteristic temperatures of solidification and decrease the segregation of refractory elements during the solidification process [23]. In addition, the formation tendency of freckle [22] and hot cracking [24] were reduced by Ta addition. These researches showed that Ta addition significantly modified the solidification behavior and further influenced the solidification microstructure and mechanical properties of nickel-base superalloys. However, the effect of Ta addition on the solidification microstructure and element segregation of a specific superalloy, IN617B alloy, has not been studied. Therefore, this study carried out microstructural observation, element segregation detection and differential thermal analysis of as-cast IN617B alloy with different Ta contents. The aim of this work is to understand and elucidate the mechanism of how Ta addition affects solidification microstructure of IN617B alloy.

2 Experimental

2.1 Materials and samples preparation

Chemical compositions of IN617B alloy are shown in Table 1. IN617B alloy with different Ta levels was produced by the vacuum induction melting followed by investment casting. The baseline alloy without Ta element was named as No.1 alloy and other alloys doped with 0.2, 0.5, 1.0 and 2.0 wt.% Ta were named as No. 2, No. 3, No. 4 and No. 5 alloy, respectively. Then, each experimental alloy was cast into the rod of 15 mm in diameter and 220 mm in length. All cast rods were cut via wire electrical discharge machining into cylinder specimens with 10 mm in length for microstructure observation. In addition, the specimens of 3 mm × 1.55 mm were also prepared for differential thermal analysis (DTA).

Table 1 Chemical compositions of IN617B alloy (wt.%)

Cr	Co	Mo	Al	Ti	Fe	C	Mn
22	12	9	1.3	0.4	1.1	0.05	0.05
Cu	B	S	Si	P	Nb	Ni	
0.04	<0.006	<0.015	<0.07	<0.012	<0.08	Bal.	

2.2 Methods

A J-MatPro Version7.0 thermodynamic calculation software was used to analyze the non-equilibrium solidification microstructure of IN617B alloy with different Ta levels. Microstructure observation and element segregation were carried out by optical microscope (OM) and scanning electron microscope (SEM, JEOL−6340) with energy dispersive spectroscopy (EDS), and energy probe microanalysis (EMPA, CAMECA SX−100). Before microstructure observations, the

surfaces of all samples were ground from 180-grit to 2000-grit and mechanically polished. Then, electrolytic etching was employed at 15 V for 30−60 s at room temperature in an electrolyte containing 300 mL HCl + 100 mL HNO_3 + 500 mL $C_3H_8O_3$. The size and area fraction of phases formed in solidification microstructures were measured by image analysis software (Image Pro Plus 6.0). At least twenty OM and SEM micrographs from different grains were selected to minimize measurement errors. Transmission electron microscope (TEM, TECNAI G2 F20) observation was conducted for identification of precipitated phase. Thin foils of 600 mm in thickness were cut from the cast rods for TEM analysis. Thin foils were then mechanically ground to 50 mm and thinned by twin-jet electro polishing in a solution of 10% perchloric acid under 20 V at −22 °C. DTA test was carried out in the integrated thermal analyzer with TG-DTA (model SETSYS Evolution18) and samples were heated up to 1450 °C employing a heating rate of 10 °C/min.

3 Results and discussion

3.1 Thermodynamic calculation

The temperature-dependent equilibrium phase fraction of IN617B alloy was obtained using the software JMatPro7.0 with Ni-based alloy database, as shown in Fig. 1. It can be found from Fig. 1(a) that the types of the predicted phases consist of γ, γ', M_3B_2, M_6C and $M_{23}C_6$ under equilibrium condition. The precipitation temperatures of these phases are listed in order as follows: $\gamma > M_3B_2 > M_6C > M_{23}C_6 > \gamma'$. This implies that the solidification path of IN617B alloy is as follows: $L \rightarrow \gamma$ matrix $\rightarrow M_3B_2 \rightarrow M_6C \rightarrow M_{23}C_6 \rightarrow \gamma'$. The non-equilibrium phase diagrams of solidification microstructures of IN617B alloy were predicated by thermodynamic calculation where the cooling rate was set at 2 °C/s, as shown in Fig. 1(b), where γ' phase is not found in non-equilibrium microstructures. Therefore, the solidification path of IN617B alloy is as follows: $L \rightarrow \gamma$ matrix $\rightarrow M_3B_2 \rightarrow M_6C \rightarrow M_{23}C_6$. The mass fractions of M_6C and $M_{23}C_6$ calculated by the thermodynamic calculation software are 0.970% and 0.198%, respectively, as shown in Fig. 1(c). Due to the addition of trace element B, the predicted content of M_3B_2 boride is very limited, which indicates that the presence of boride is hard to be observed in microstructure observation. This

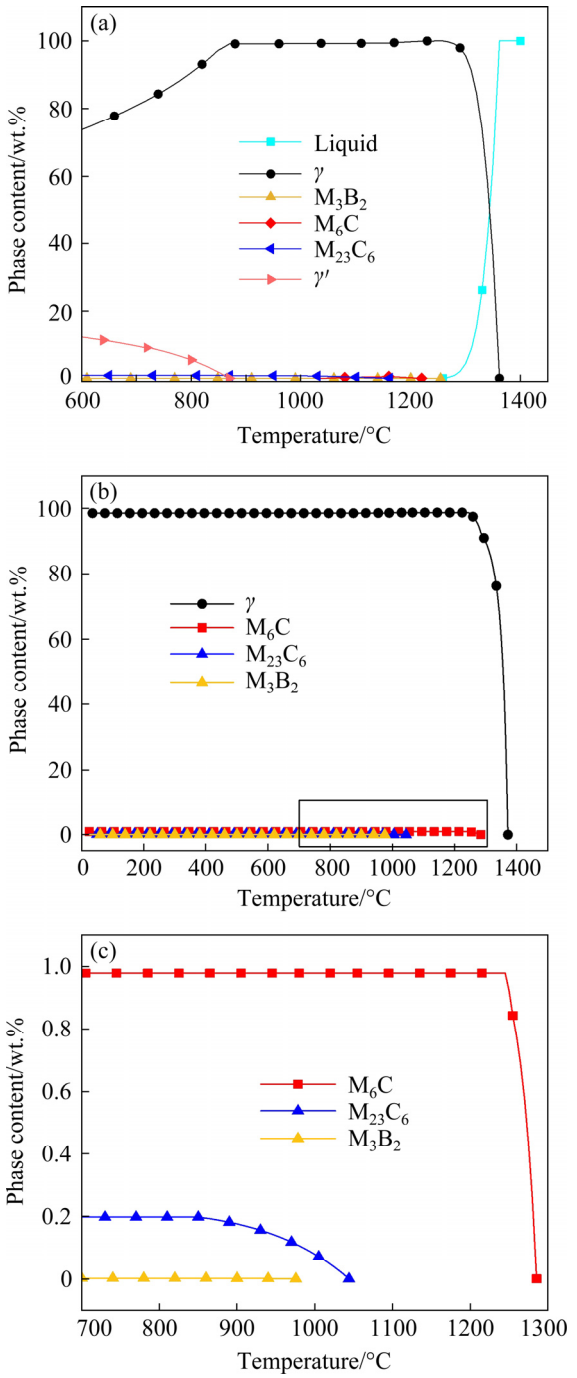

Fig. 1 Thermodynamic calculation results of IN617B alloy without Ta: (a) Equilibrium phase diagram; (b) Non-equilibrium phase diagram of solidification microstructures; (c) Magnified diagram of part in (b)

boride was also proved by TYTKO et al [14] using Thermo-Calc soft and whereas they did not found M_3B_2 boride in long-term aging microstructure by a high angle annular dark field detector. Moreover, they deemed that B replaced a little C in $M_{23}C_6$ forming $M_{23}(B, C)_6$ and they found lots of B enriched at the $M_{23}C_6/\gamma$ and $M_{23}C_6/\gamma'$ phase interface.

Figure 2 shows the dependence of the content of different phases on Ta content which is obtained by thermodynamic calculation. It can be seen that the precipitation of a new phase MC is initiated when the content of Ta is more than 0.5 wt.%. In addition, the content of MC increases with Ta content increasing while M_6C content is obviously reduced and $M_{23}C_6$ content is slightly decreased. This indicates that the addition of Ta contributes to the formation of MC carbides from the melt of IN617B alloy. Moreover, Ta addition can suppress the formation of M_6C carbides, because the prior formation of MC carbides consumed a large number of C element. The appropriate level of MC is effective to improve the mechanical properties and microstructural stability of alloy due to the relatively stability of Ta-rich MC at elevated temperatures [25,26]. It can be speculated from the above thermodynamic calculation result that Ta addition will change the constitute of primary phases in solidification microstructure and even impact the microstructural stability of alloys during the long-term and high-temperature service.

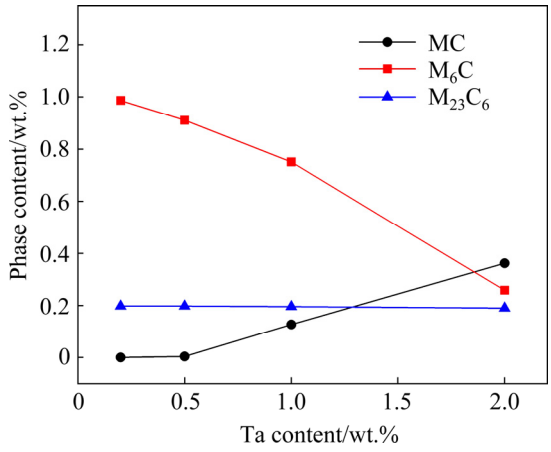

Fig. 2 Effect of Ta on content of carbides in IN617B alloy

3.2 Solidification microstructures

The solidification microstructures of No. 1 alloy without Ta element are shown in Fig. 3. The typical dendritic microstructures are observed in the solidification microstructures from OM and SEM images (Figs. 3(a) and (b)), in which the distance between the secondary dendrites is about 96 μm, indicating that the alloy has obvious element segregation. The grain size was calculated according to the national GB 6394—2002 standard. The average grain size is 850 μm and the macroscopic grain grade number is M-11. It can be seen from Fig. 3(b) that the primary carbides are mainly distributed in the interdendritic region. In addition, GBs are filled with a large number of carbides which are mainly composed of mesh-like M_6C, lath-shaped $M_{23}C_6$ and black granular Ti(C, N), as shown in Fig. 3(c). According to the EDS analysis results (Table 2), it is found that M_6C is Mo-rich carbide, $M_{23}C_6$ is Cr-rich carbide, and

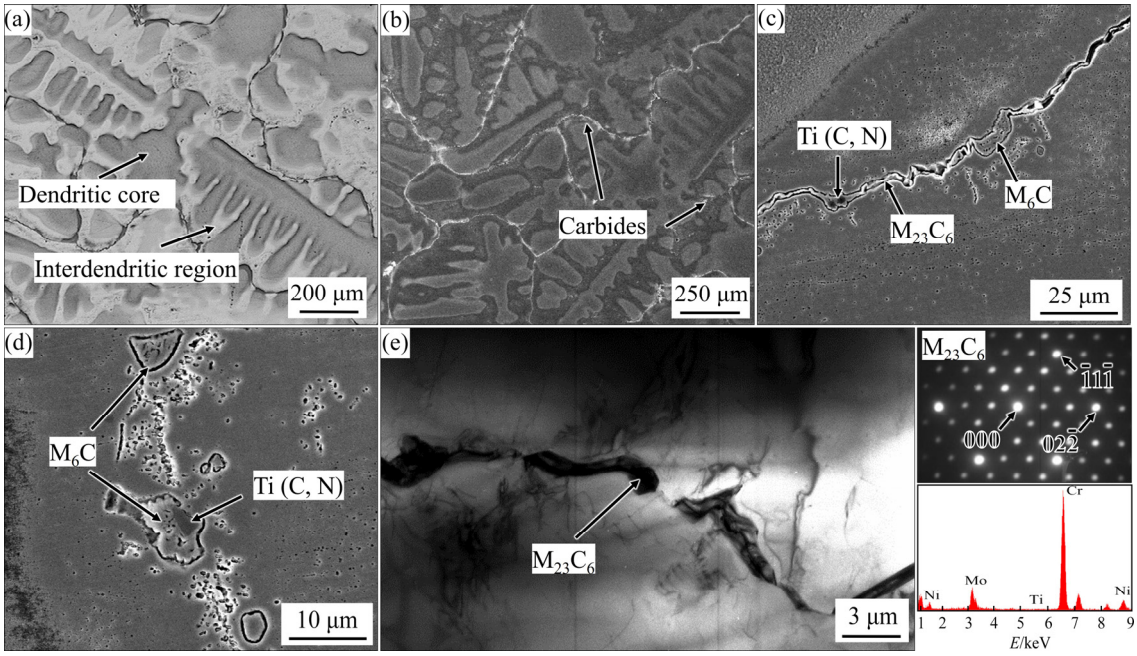

Fig. 3 Solidification microstructures of No.1 alloy: (a, b) OM and SEM images of dendritic microstructure; (c, d) SEM images of inter- and intra-granular carbides; (e) TEM image with SAED pattern and EDS spectrum of carbide at GBs

Ti(C, N) is Ti-rich carbonitride. The observation result is consistent with previous studies [10,16,17]. However, the existence of Ti(C,N) precipitate was not predicted in the thermodynamic calculation due to the chemical composition without nitrogen of IN617B alloy entered into J-MatPro Version7.0 software. During the actual nickel-base superalloy melting and solidifying process, the nitrogen from raw materials or processing conditions is difficult to be removed. And nitrogen element has a strong affinity with some strengthening elements (such as Cr, Al, Ti, and Nb) forming common nitrides with the relatively stability [16,27].

Table 2 Chemical compositions of primary precipitates in No.1 alloy microstructure (wt.%)

Phase	Al	Ti	Cr	Co	Ni	Mo
Ti(C,N)	0.42	72.2	5.15	2.04	4.82	11.97
M_6C	0.1	1.32	27.65	2.68	5.42	65.37
$M_{23}C_6$	0.21	0.77	35.32	10.56	40.45	14.13

From Fig. 3(d), it can be seen that mesh-like M_6C and black Ti(C,N) distribute inside grains and the two precipitates are easy to form symbiotic microstructure, where M_6C precipitated on the surface of Ti(C,N). Figure 3(e) shows TME morphology of the GB in the solidification microstructures of No.1 alloy. According to the corresponding selected area electron diffraction (SAED) pattern and EDS energy spectrum, it is determined that lath-shaped $M_{23}C_6$ has a face-centered cubic (FCC) crystal structure with a lattice parameter of a=1.03 nm.

Figure 4 shows the OM morphologies of solidification microstructures of four alloys with different Ta contents. The dendritic microstructure is also observed clearly in four alloys. Moreover, it can be seen that the solidification microstructure morphologies of four alloys are identical regardless of the difference in Ta content. However, it is found that the secondary dendrite arm spacings decrease from 92.1 to 73.9 μm (Table 3) with the Ta content increasing from 0.2 to 2.0 wt.%. The alloying element segregation is considered to be the essential reason of the formation of the dendritic morphology. Therefore, the decreasing secondary dendrite arm spacings implies that the Ta addition can relieve the alloying element segregation.

Figure 5 shows the SEM morphology of the solidification microstructure of four alloys. The primary carbides with gray contrast are observed to exhibit island-shape distributed in the interdendritic region. It can be found that the number of these islands gradually decreases with the increase of Ta content. Meanwhile, the area fractions of these islands decrease from 0.79% to 0.66% with the increase of Ta content (Table 3). The island-shape carbides include all primary carbides, such as MC, M_6C and $M_{23}C_6$. Therefore, the reduced area fraction of islands indicates that the total content of primary carbides precipitated in solidification microstructure gradually decreases. The precipitation of primary carbides can effectively inhibit the growth of grain by hindering the movement of GBs. Therefore, it is inferred that the inhibition effect is impaired due to the Ta addition. The conclusion is testified by the experimental data (Table 3), which shows that the grain size of the solidification microstructure increases slightly from 0.88 to 1.09 mm with the Ta content increasing to 2.0 wt.%.

Backscattered electron images (BSEM) were used to distinguish the type of primary carbide within grains and at GBs, as shown in Fig. 6. The white contrast of MC carbide is observed in BSEM image due to lots of heavy metal element Ta with high atomic number. The morphology of mesh-like M_6C in the alloys with Ta element is same to that in No.1 alloy. Meanwhile, lots of particles precipitates distributed around mesh-like M_6C in No.1 alloy (Fig. 3(d)) are also found in the alloys with Ta

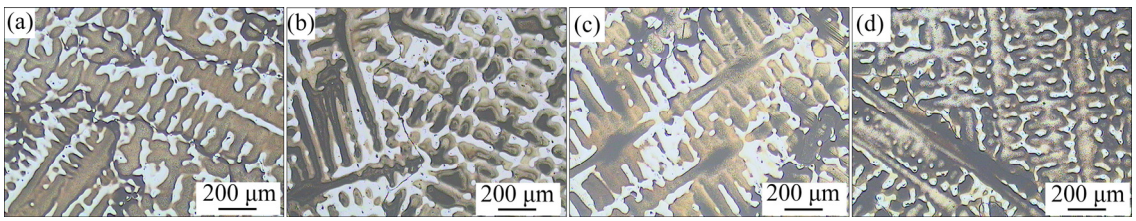

Fig. 4 OM images of solidification microstructure of four alloys: (a) No.2 alloy with 0.2 wt.% Ta; (b) No.3 alloy with 0.5 wt.% Ta; (c) No.4 alloy with 1.0 wt.% Ta; (d) No.5 alloy with 2.0 wt.% Ta

Table 3 Average grain size, secondary dendritic arm spacing and total area fraction of carbide in four alloys with different Ta contents

Alloy No.	Average grain size/mm	Secondary dendrite arm spacing/μm	Total area fraction of carbide/%
2	0.88±0.02	92.1±0.5	0.79±0.02
3	0.96±0.01	90.8±0.3	0.78±0.01
4	1.02±0.03	80.3±0.6	0.72±0.02
5	1.09±0.02	73.9±0.5	0.66±0.03

Note: The standard errors of values were calculated by the standard deviation formula

element and they are identified as Mo-rich M_6C carbide according to the EDS line analysis results in Fig. 6(a). It is found from Figs. 6(b−d) that the black Ti(C,N) in the symbiotic microstructure of M_6C and Ti(C,N) (Fig. 3(d)) is replaced by white Ta-rich MC. Moreover, the black Ti(C,N) is hard to discover in the alloys with Ta element above 0.5 wt.%. This signifies that the binding capacity between Ta and C is stronger than that between Ti and C or N. Therefore, the preferential precipitation of Ta-rich MC suppresses the precipitation of Ti(C,N) when Ta is enough. In addition, it is also found that Ta-rich MCs appear at GBs, preventing the formation of continuous lath-shaped $M_{23}C_6$ at GBs which is considered to damage the strength of GBs, as shown in Figs. 6(f−h). The size and area fraction of MC are listed in Table 4, which shows that the size and area fraction increase obviously with Ta content increasing. This indicates that the Ta addition significantly promotes the precipitation of primary MC carbide, which is agreement with the previous thermodynamic calculation.

The symbiotic microstructure of M_6C and Ti(C,N) or MC is observed in both the alloys with Ta and without Ta, which was not reported in previous study of IN617B alloy [28−30]. The formation of the symbiotic microstructure is further analyzed through the mechanism model of the symbiotic structure established in Fig. 7. During the solidification process, MC carbides will preferentially nucleate and grow up since the binding ability of Ta with C is stronger than that of Mo or Cr with C. Mo and Cr are the main formation elements of M_6C (Table 2). Due to MC depleting Mo and Cr, the two elements are rejected into the γ

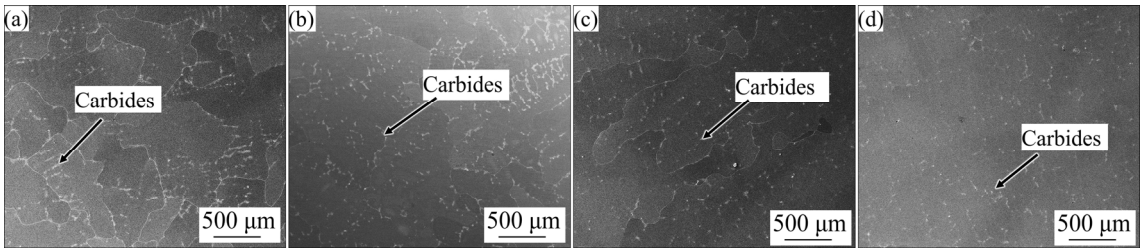

Fig. 5 SEM images of solidification microstructure of four alloys: (a) No.2 alloy with 0.2 wt.% Ta; (b) No.3 alloy with 0.5 wt.% Ta; (c) No.4 alloy with 1.0 wt.% Ta; (d) No.5 alloy with 2.0 wt.% Ta

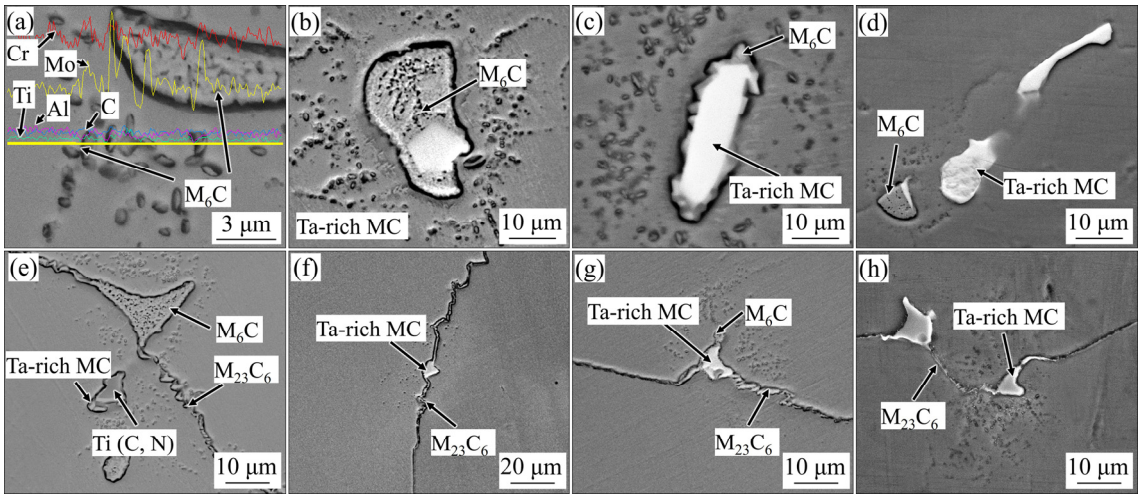

Fig. 6 BSEM morphologies of carbides within grains and at GBs for four alloys: (a, e) No.2 alloy with 0.2 wt.% Ta; (b, f) No.3 alloy with 0.5 wt.% Ta; (c, g) No.4 alloy with 1.0 wt.% Ta; (d, h) No.5 alloy with 2.0 wt.% Ta

Table 4 Area fraction and average size of MC carbide

Alloy No.	MC area fraction/%	MC average size/μm
2	0.08±0.05	3.21±0.02
3	0.12±0.02	5.13±0.03
4	0.24±0.03	5.59±0.01
5	0.30±0.06	8.40±0.05

matrix surrounding MC When MC preferentially precipitates. Subsequently, the concentrations of Mo and Cr near MC gradually rise, contributing to the formation of M_6C on the surface of MC, where the involved reaction formula is as follows: γ matrix + MC → MC + M_6C. Similarly, this is also the formation mechanism of symbiotic microstructure of M_6C and Ti(C,N) in the alloy without Ta, since Ti binds with C and N more easily comparing with other metal elements (Mo and Cr) in the molten metal [31], resulting in the preferent formation mechanism of Ti(C,N).

3.3 Alloying element distribution

Figure 8 shows BSEM image and EPMA element distribution mappings in dendritic microstructure of No. 1 alloy. It is seen that the segregation behavior of different elements in No.1 alloy is obviously different. There is no obvious segregation of Cr element. Ni and Co are slightly segregated in the dendrite core while Mo and Ti obviously are segregated in the interdendritic region. The concentration of alloying elements in the dendrite core and interdendritic region was detected by EPMA, and the segregation coefficient k was then calculated according to the formula of $k=C_D/C_I$, where C_D represents the content of an element in the dendrite core, and C_I represents the content of an element in the interdendritic region. The values of C_D, C_I and k of five alloys with different Ta contents are listed in Table 5. It can be found that the k values of Al, Ti, Mo and Ta are lower than 1, which indicates that these alloying elements are ejected to the front of liquid−solid interface and finally diffused to the interdendritic region during solidification process. Moreover, the k values of Al, Ti and Mo increase and become close to 1 with Ta content increasing while the k value of Ta decreases from 0.83 to 0.54. This signifies that the Ta addition can reduce the segregation level of Al, Ti and Mo, but lead to enhancing the segregation of Ta to the interdendritic region. In addition, it is found that the Ta addition has no obvious effect on the segregation level of the alloying elements (Co and Ni) segregated in the dendrite core, because their k values have no change with Ta content increasing. It is known that the alloying element segregation is the essential

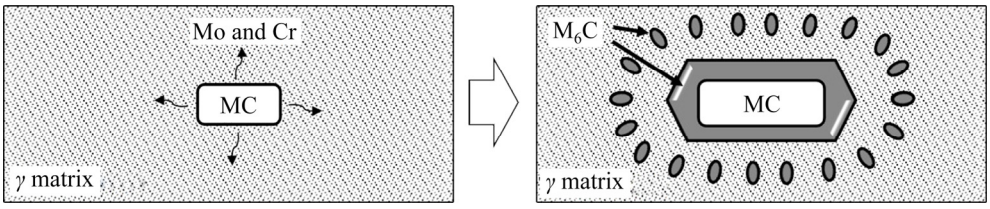

Fig. 7 Mechanism model of symbiotic structure of MC and M_6C carbide during solidification

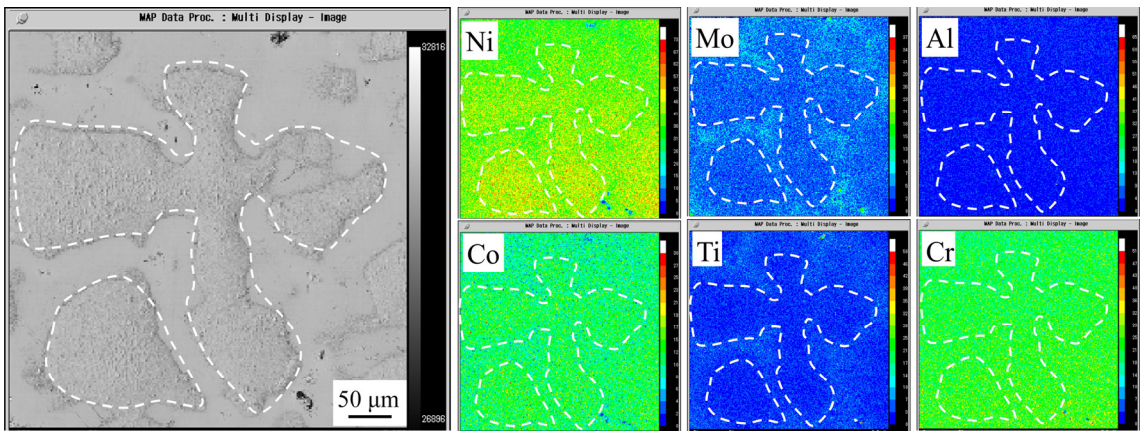

Fig. 8 BSEM image and EPMA element distribution mappings of No.1 alloy

Table 5 Contents of main alloying elements in dendrite core and interdendritic region and portioning coefficients (k) in five alloys

Alloy No.		Al	Ti	Cr	Co	Ni	Mo	Ta
1	C_D/wt.%	1.13	0.23	21.69	12.83	56.33	7.7	−
	C_I/wt.%	1.65	0.44	22.45	11.7	52.51	11.27	−
	k	0.69	0.52	0.97	1.06	1.03	0.71	−
2	C_D/wt.%	1.24	0.24	21.74	12.38	55.33	7.17	0.51
	C_I/wt.%	1.5	0.31	22.45	11.72	53.6	10.1	0.62
	k	0.83	0.77	0.97	1.06	1.03	0.71	0.83
3	C_D/wt.%	1.17	0.24	22.33	12.46	55.4	8.15	0.67
	C_I/wt.%	1.42	0.35	22.37	11.19	52.84	10.99	0.85
	k	0.82	0.67	1	1.11	1.05	0.74	0.79
4	C_D/wt.%	1.1	0.25	22.11	12.54	55.76	7.92	0.89
	C_I/wt.%	1.24	0.29	22.3	11.48	54.11	9.32	1.27
	k	0.89	0.84	0.99	1.09	1.03	0.85	0.7
5	C_D/wt.%	1.17	0.22	22	12.14	55.18	7.79	1.58
	C_I/wt.%	1.28	0.25	22.67	10.86	53.59	9.06	2.91
	k	0.91	0.88	0.97	1.12	1.03	0.86	0.54

reason of the formation of dendritic morphology in solidification microstructure. Therefore, it is deemed that the mitigated segregation of Al, Ti and Mo contributes to the decrease of secondary dendrite arm spacings with Ta content increasing, which is observed in the solidification microstructures section.

3.4 Solidification characteristic temperature

The relevant characteristic temperatures during the alloy solidification process are obtained from DTA heating curves, as listed in Table 6. Based on the results of the solidification microstructure and previous reports [12,32] about the temperature of carbide transformation, it can be determined that T_1, T_2 and T_3 should correspond to the melting point peaks of primary $M_{23}C_6$, M_6C and MC or Ti(C,N), respectively. Moreover, T_S and T_L represent the solidus and liquidus temperature, respectively. The order of the characteristic temperatures is $T_L > T_S > T_3 > T_2 > T_1$. It can be seen from Table 6 that T_3 gradually decreases from 1293 to 1205 °C with the increase of Ta content while T_1 and T_2 have no distinct change. At the same time, the solidification temperature range (T_S−T_L) slightly decreases from 30 to 25 °C with T_S and T_L increasing. Although the T_3 decreases evidently due to the Ta addition, the order of the characteristic temperatures has no change. This indicates that the Ta addition has no obvious effect on the solidification path of IN617B alloy, that is, $L \rightarrow \gamma$ matrix → MC or Ti(C,N) → M_6C → $M_{23}C_6$.

Table 6 Phase transformation temperatures and solidification temperature range for five alloys

Alloy No.	T_S/°C	T_L/°C	T_1/°C	T_2/°C	T_3/°C	(T_S−T_L)/°C
1	1365	1393	979	1079	1293	28
2	1363	1393	963	1079	1278	30
3	1365	1395	972	1077	1253	30
4	1370	1399	973	1075	1229	29
5	1371	1396	976	1078	1205	25

4 Conclusions

(1) The solidification microstructure of IN617B alloy shows a typical dendritic morphology with primary M_6C, $M_{23}C_6$ and Ti(C,N) phase distributed in the interdendritic region. Ni and Co are slightly segregated in dendrite cores while Al, Mo and Ti are obviously segregated in interdendritic regions.

(2) The Ta addition promotes the precipitation of primary Ta-rich MC, resulting in the decreased

content of M_6C and $M_{23}C_6$. The Ta addition mitigates the segregation of Al, Mo and Ti, and subsequently decreases the secondary dendrite spacing.

(3) Although the Ta addition decreases the melting temperature of MC, it has no effect on the solidification path of IN617B alloy as follows: $L \rightarrow \gamma$ matrix → MC or Ti(C,N) → M_6C → $M_{23}C_6$. MC and Ti(C,N) tends to form symbiotic microstructure with M_6C carbide.

Acknowledgments

This work was supported by Shanghai Sailing Program, China (No. 19YF1417500). The authors thank Yong-hua RONG from Shanghai Jiaotong University for fruitful discussion, and Yong-an GUO for preparing the experimental samples, Mei-shuai LIU for language polishing

References

[1] FAN Hao-jie, ZHANG Zhong-xiao, DONG Jian-cong, XU Wei. China's R&D of advanced ultra-supercritical coal-fired power generation for addressing climate change [J]. Thermal Science and Engineering Progress, 2018, 5(1): 364−371.

[2] YANG Fei, HOU Jie-shan, WANG Chang-shuai, ZHOU Lan-zhang. Effects of solution treatment on microstructure and tensile properties of as-cast alloy 625 [J]. Transactions of Nonferrous Metals Society of China, 2021, 31(2): 426−437.

[3] BUGGE J R, KJÆR S, BLUM R. High-efficiency coal-fired power plants development and perspectives [J]. Energy, 2006, 31(10/11): 1437−1445.

[4] LI Shan-lin, LI Ke-jian, CAI Zhi-peng, PAN Ji-luan. Behavior of M23C6 phase in Inconel 617B superalloy during welding [J]. Journal of Materials Processing Technology, 2018, 258(8): 38−46.

[5] GIBBONS T B. Superalloys in modern power generation applications [J]. Materials Science and Technology, 2009, 25(2): 129−135.

[6] ZHANG Yu, JING Hong-yang, XU Lian-yong, HAN Yong-dian, ZHAO Lei, LI Hai-zhou, TANG Zheng-xin, TONG Tian-wang. Microstructure and grain boundary engineering of a novel Fe−Cr−Ni alloy weldment made with self-developed composition-matched weld filler metal [J]. Transactions of Nonferrous Metals Society of China, 2020, 30(4): 992−1004.

[7] KLÖWER J, HUSEMANN R U, BADER M. Development of nickel alloys based on alloy 617 for components in 700 °C power plants [J]. Procedia Engineering, 2013, 55(3): 226−231.

[8] GAO Shuang, HE Bo, ZHOU Lan-zhang, HOU Jie-shan. Effects of Ta on the high temperature oxidation behavior of IN617 alloy in air [J]. Corrosion Science, 2020, 170(7): 108682.

[9] SUN Li-ling, DONG Lian-ke, ZHANG Ji-shan, TANG Ya-jun, ZHANG Jing-hua, HU Zhuang-qi. Fractal analyses of directional solidification behavior of a Ni-base superalloy [J]. Acta Metallurgica Sinica (English Letters), 1993, 29(3): 19−24.

[10] WU Quan-yan, SONG H, SWINDEMAN R W, SHINGLEDECKER J P, VASUDEVAN V K. Microstructure of long-term aged IN617 Ni-base superalloy [J]. Metallurgical and Materials Transactions A, 2008, 39(11): 2569−2585.

[11] DI MARTINO S F, FAULKNER R G, HOGG S C, VUJIC S, TASSA O. Characterisation of microstructure and creep properties of alloy 617 for high-temperature applications [J]. Materials Science and Engineering A, 2014, 619(6): 77−86.

[12] KRISHNA R, HAINSWORTH S V, GILL S P A, STRANG A, ATKINSON H V. Topologically close-packed μ phase precipitation in creep-exposed Inconel 617 alloy [J]. Metallurgical and Materials Transactions A, 2013, 44(3): 1419−1429.

[13] GARIBOLDI E, CABIBBO M, SPIGARELLI S, RIPAMONTI D. Investigation on precipitation phenomena of Ni−22Cr−12Co−9Mo alloy aged and crept at high temperature [J]. International Journal of Pressure Vessels and Piping, 2008, 85(1/2): 63−71.

[14] TYTKO D, CHOI P P, KLÖWER J, KOSTKA A, INDEN G, RAABE D. Microstructural evolution of a Ni-based superalloy (617B) at 700 °C studied by electron microscopy and atom probe tomography [J]. Acta Materialia, 2012, 60(4): 1731−1740.

[15] TAN L, YANG Y, NANSTAD R K, BUSBY J T. Effect of thermal aging on coarsening kinetics of γ' in alloy 617 [J]. Journal of Phase Equilibria and Diffusion, 2014, 35(5): 524−529.

[16] KRISHNA R, ATKINSON H V, HAINSWORTH S V, GILL S P. Gamma prime precipitation, dislocation densities, and TiN in creep-exposed Inconel 617 alloy [J]. Metallurgical and Materials Transactions A, 2016, 47(1): 178−193.

[17] ISPÁNOVITY P D, BAKÓ B, WEYGAND D, HOFFELNER W, SAMARAS M. Impact of gamma′ particle coarsening on the critical resolved shear stress of nickel-base superalloys with low aluminium and/or titanium content [J]. Journal of Nuclear Materials, 2011, 416(1/2): 55−59.

[18] GAO Shuang, HOU Jie-shan, YANG Fei, GUO Yong-an, ZHOU Lan-zhang. Effect of Ta on microstructural evolution and mechanical properties of a solid-solution strengthening cast Ni-based alloy during long-term thermal exposure at 700 °C [J]. Journal of Alloys and Compounds, 2017, 729(12): 903−913.

[19] TAN Yuan-guo, LIU Fang, ZHANG An-wen, HAN Da-wei, YAO Xiao-yu, ZHANG Wei-wei, SUN Wen-ru. Element segregation and solidification behavior of a Nb, Ti, Al Co-strengthened superalloy ЭК151 [J]. Acta Metallurgica Sinica (English Letters), 2019, 32(10): 1298−1308.

[20] MENG Zhao-yu, SUN Gen-chang, LI Min-lun, XIE Xi-shan. The strengthening effect of tantalum in nickel-base superalloys [C]// Superalloys Warrendale, PA: TMS, 1984: 563−572.

[21] TSAI Y L, WANG S F, BOR H Y, HSU Y F. Effects of alloy elements on microstructure and creep properties of fine-grained nickel-based superalloys at moderate

temperatures [J]. Materials Science and Engineering A, 2013, 571(6): 155−160.
[22] REED R C, TAO T, WARNKEN N. Alloys-by-design: Application to nickel-based single crystal superalloys [J]. Acta Materialia, 2009, 57(19): 5898−5913.
[23] MA Shi-hua, HAO Hong-quan, WANG Dong, LOU Lang-hong, ZHANG Jian. Effects of Ta on the solidification behavior and microstructure of a rhenium-containing hot corrosion resistant single crystal [J]. International Journal of Minerals, Metallurgy, and Materials, 2019, 26(7): 901−907.
[24] ZHANG Jian. Effect of Ti and Ta on hot cracking susceptibility of directionally solidified Ni-based superalloy IN792 [J]. Scripta Materialia, 2003, 48(6): 677−681.
[25] ZHENG Liang, ZHANG Guo-qing, LEE T L, GORLEY M J, WANG Yue, XIAO Cheng-bo, LI Zhou. The effects of Ta on the stress rupture properties and microstructural stability of a novel Ni-base superalloy for land-based high temperature applications [J]. Materials & Design, 2014, 61(9): 61−69.
[26] BRINEGAR J R, MIHALISIN J R, VANDERSLUIS J. The effects of tantalum for columbium substitutions in alloy 713C [C]//Superalloys, 1984: 53−61.
[27] YIN Feng-shi, SUN Xiao-feng, LI Jin-guo, GUAN Heng-rong, HU Zhi-qing. Preparation of a (Ti,Nb,W)C particulate reinforced nickel-base superalloy via super-high temperature treatment of melt [J]. Materials Letters, 2003, 57(22/23): 3377−3380.
[28] KRISHNA R, HAINSWORTH S V, ATKINSON H V, STRANG A. Microstructural analysis of creep exposed IN617 alloy [J]. Materials Science and Technology, 2010, 26(7): 797−802.
[29] MANKINS W L, HOSIER J C, BASSFORD T H. Microstructure and phase stability of INCONEL alloy 617 [J]. Metallurgical and Materials Transactions B, 1974, 5(12): 2579−2590.
[30] GUO Yan, ZHANG Zhou-bo, ZHOU Rong-can, HOU Shu-fang, WANG Bo-han. Microstructure and mechanical properties of alloy 617B [J]. Transactions of Nonferrous Metals Society of China, 2015, 25(4): 1106−1113.
[31] PETROVA L G, CHUDINA O V. Evaluation of dispersion hardening by various coherent nitrides in nitriding alloys based on iron, nickel, and cobalt [J]. Metal Science and Heat Treatment, 1999, 41(6): 238−241.
[32] GUI Wei-min, ZHANG Xiao-tian, ZHANG Hong-yu, SUN Xiao-feng, ZHENG Qi. Melting of primary carbides in a cobalt-base superalloy [J]. Journal of Alloys and Compounds, 2019, 787(5): 152−157.

Ta 对 IN617B 镍基高温合金凝固组织及元素偏析的影响

高 双[1,2]，宋振峰[1,2]，何 博[1,2]，周兰章[3]，侯介山[3]

1. 上海工程技术大学 材料工程学院，上海 201620；
2. 上海工程技术大学 高温合金精密成型研究中心，上海 201620；
3. 中国科学院 金属研究所，沈阳 110016

摘 要：IN617B 镍基高温合金是 700 °C 先进超超临界燃煤电站的主要候选材料。采用 OM、SEM、TEM、EDS、EPMA 和热力学计算等方法研究 Ta 对 IN617B 镍基高温合金凝固行为及组织的影响。研究结果表明：IN617B 合金的凝固组织呈典型的树枝晶形貌，在枝晶间和晶界处分布着网状的 M_6C、板条状的 $M_{23}C_6$ 和颗粒状的 Ti(C,N)；Ta 的加入促进富 Ta 的 MC 碳化物的析出，显著抑制 M_6C 和 $M_{23}C_6$ 的析出，并且降低合金元素 Al、Mo 和 Ti 的偏析程度；Ta 的加入明显降低 MC 碳化物的析出温度，但未改变合金的凝固路径：$L\rightarrow\gamma\rightarrow$ MC 或 Ti(C,N) $\rightarrow M_6C\rightarrow M_{23}C_6$，在凝固过程中 MC 和 Ti(C,N)易与 M_6C 碳化物形成共生组织。该研究为 IN617B 镍基高温合金的合金优化和铸造组织调控提供理论基础和数据支持。

关键词：IN617B 镍基高温合金；Ta 添加；凝固组织；成分偏析；碳化物

(Edited by Xiang-qun LI)